



**HAL**  
open science

# Heat extremes in Western Europe are increasing faster than simulated due to missed atmospheric circulation trends

R. Vautard, J. Cattiaux, T. Happé, J. Singh, R. Bonnet, C. Cassou, D. Coumou, F. D'Andrea, Davide Faranda, E. Fischer, et al.

► **To cite this version:**

R. Vautard, J. Cattiaux, T. Happé, J. Singh, R. Bonnet, et al.. Heat extremes in Western Europe are increasing faster than simulated due to missed atmospheric circulation trends. 2023. hal-04266530v1

**HAL Id: hal-04266530**

**<https://hal.science/hal-04266530v1>**

Preprint submitted on 13 Jan 2023 (v1), last revised 31 Oct 2023 (v4)

**HAL** is a multi-disciplinary open access archive for the deposit and dissemination of scientific research documents, whether they are published or not. The documents may come from teaching and research institutions in France or abroad, or from public or private research centers.

L'archive ouverte pluridisciplinaire **HAL**, est destinée au dépôt et à la diffusion de documents scientifiques de niveau recherche, publiés ou non, émanant des établissements d'enseignement et de recherche français ou étrangers, des laboratoires publics ou privés.

# Heat extremes in Western Europe are increasing faster than simulated due to missed atmospheric circulation trends

R. Vautard[1], J.Cattiaux[2], T. Happé[3], J. Singh [4], R. Bonnet[1], C. Cassou[5], D. Coumou[3,1,8], F. D'Andrea[6], D. Faranda[7], E. Fischer [4], A. Ribes[2], S. Sippel [4], P. Yiou[7]

[1] Institut Pierre-Simon Laplace, CNRS, Université Paris-Saclay, Sorbonne Université, France

[2] Centre National de Recherches Météorologiques, Université de Toulouse, Météo-France, CNRS, Toulouse, France.

[3] Institute for Environmental Studies, Vrije Universiteit Amsterdam, Amsterdam, Netherlands

[4] Institute for Atmospheric and Climate Science, ETH Zurich, Zürich, Switzerland

[5] Centre Européen de Recherche et de Formation Avancée en Calcul Scientifique, CNRS UMR 5318, Toulouse, France

[6] Laboratoire de Météorologie Dynamique, IPSL, CNRS, Paris, France

[7] Laboratoire des Sciences du Climat et de l'Environnement, UMR 8212 CEA-CNRS-UVSQ, Université Paris-Saclay and IPSL, 91191 Gif-sur-Yvette, France

[8] Royal Netherlands Meteorological Institute (KNMI), De Bilt, Netherlands

## Abstract

**Over the last 70 years, extreme heat has been increasing at global scale [1,2], with a rapid rate in several regions including Western Europe [3]. Climate models broadly capture heat trends globally [1], but exhibit systematically weaker extreme heat trends than observations in Western Europe [4-6], together with a weaker summer warming [7,8]. The causes of this mismatch, confirmed here by the analysis of 273 latest generation coupled climate simulations, among which only a handful of them overpass observed trends, are not well understood. Here we use a circulation analogue approach [9,10] to identify the dynamical contribution to temperature trends [11-12], and show that a substantial fraction (1.0°C [0.4°-1.6°C] of 3.4°C per global warming degree) of the trend is due to circulation changes, largely due to increases in southerly flows over Western Europe. Their rapid increase in frequency (+63% [20%-106%] since 1950) and persistence (+45% [12%-77%]) are not captured by any of the 32 climate model flow simulations analyzed. The few simulations reaching the observed warming trends in extreme heat have weak dynamical changes, with a decrease in occurrence of southerly flows, indicating that they capture the warming trend for the wrong reasons. These model biases in circulation trends can be due to a systematically underestimated or erroneous representation of the circulation response to external forcing, or to a systematic underestimation of interdecadal variability, or both. The former implies that projections are too conservative, the latter that we are left with deep uncertainty regarding the pace**

**of future summer heat in Europe: the current strong recent trend could weaken or increase in future decades. This calls for caution when interpreting climate projections of heat extremes over Western Europe, in particular in view of adaptation to heat waves.**

Summer temperatures and heat extremes in Western Europe have warmed much faster than elsewhere in the mid-latitudes over the last two decades [3,5]. As a consequence, several unprecedented heatwaves took place in the last 20 years. In 2003, the full summer season mean temperature was unprecedented in Europe [13]. Northwestern Europe was hit by record temperatures in 2018 [14,15]. In 2019, two short (3-day) but intense heat waves saw all-time temperature records broken in many places, associated with a rapid northward advection of Saharan air [6]. All-time records were broken again in 2022, with temperatures above 40°C reaching far north (eg. Brittany, U.K.) [16]. Unprecedented, and even record-shattering extremes are plausible in climate projections [17], but the pace of their increasing magnitude in Western Europe is generally not predicted by these climate models [4,18].

Here we focus on summer (JJA) maximum and mean of daily maximal temperatures (resp. denoted hereafter TXx and TXm for simplicity), and the regional amplification of their trends relative to the global temperature trend. We verified that our results remain valid for linear trends relative to time, but do not describe them here. Trends in TXx and TXm are calculated over the 73-year 1950-2022 period using a linear regression with the Global mean Surface Air Temperature (GSAT, see methods section) from ERA5, and are expressed in °C per global warming degree (GWD). As shown in Figure 1 and Supp. Fig. 2, both ERA5 reanalyses [19] and E-OBS interpolated observations [20] show trends reaching more than 5°C/GWD for TXx in northern France and Benelux. Over the limited area spanning 5W-15E; 45N-55N (blue box, called hereafter “Western Europe”), the land area-average TXx trend is 3.4°C/GWD for ERA5 and E-OBS [2.4 - 4.3°C/GWD]. It exceeds the more moderate TXm trends by about 40% for ERA5 (2.4°C/GWD [1.7 - 3.0°C/GWD]) and 30% for E-OBS (2.6°C/GWD [1.9 - 3.3°C/GWD]).

A variety of processes have been proposed for explaining these overproportional warming trends with respect to global temperature change. For mean summer temperatures, changes in mean atmospheric circulation [7,21], changes in aerosol [22] and changes in early summer soil moisture [23] and related feedbacks were considered for explaining (part of) the trends. For extreme heat, the increase in the frequency and persistence of splitted midlatitude jet states over the last 40 years, possibly associated with the reported weakening of the mean summer zonal circulation [24], can explain about a third of the amplified trend in heatwave intensity [3]. Changes in atmospheric circulations around Europe that favor heat were also emphasized [25], in particular a positive trend in a dipole structure with a low pressure over the Eastern Atlantic [26-27] and a high pressure over the Mediterranean extended towards central Europe [28]. Yet, no increasing trend was found in blocking over Scandinavia that has led to the 2018 heat wave [14,29]. Moreover, reported changes in Rossby waves are not robust and sensitive to their exact definition [30]. In addition, variability of summer temperatures has been shown to be large in Central Europe [31]. Thus, while several studies have hinted at a potential role

of dynamical changes in amplifying European heat waves, a systematic analysis is lacking, including also how models simulate these changes.

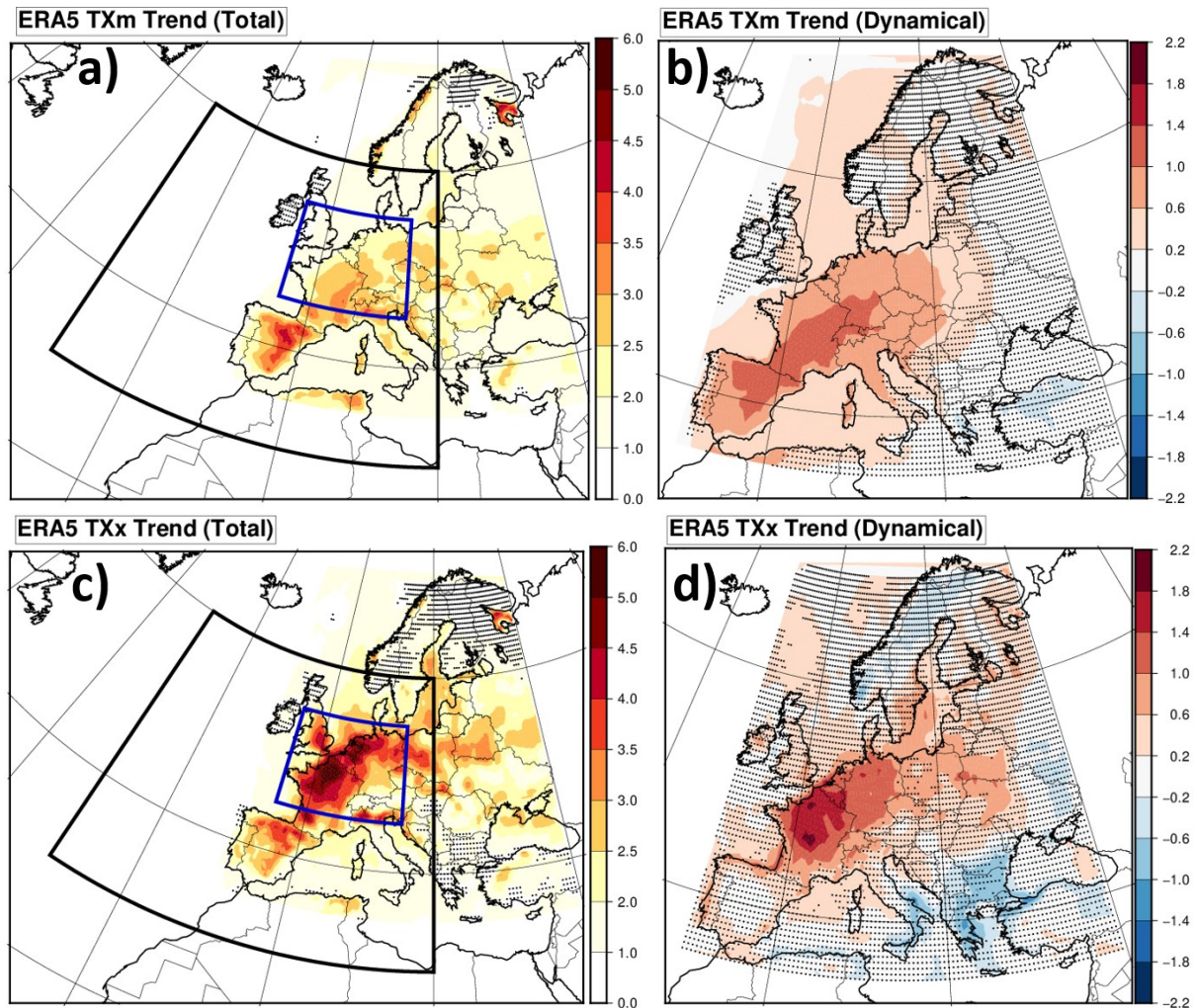


**Figure 1:** ERA5 temperature trends relative to the global warming level ( $^{\circ}\text{C}/\text{GWD}$ ), for summer Mean daily Tmax (TXm) (top row) and summer Maximum Tmax (TXx, bottom row). The raw trend (left panels) is compared to the estimated dynamical contribution to these trends (right panels), obtained by replacing daily temperatures by those of best circulation analogues with a thermodynamic correction (see Methods). The areas highlighted are: (black frame) the area used to calculate the anomaly correlation of 500 hPa streamfunction for the definition of analogues; the Western Europe focus area, where maximal daily temperature trends are averaged in this study. Dotted points show areas where statistical significance of trends is less than 95% (two sided). The statistical test uses a 2-sigma rule for the regression coefficient, accounting for the total number of well-separated analogues (see Methods).

We used a method based on circulation analogues to assess the role of dynamical changes in the TXm and TXx trends (see the methods section for a full description). Regional atmospheric circulation patterns are characterized by their 500 hPa streamfunction over the domain shown in Fig. 1a (black box). We identify circulation analogues for a given day by searching for other summer dates (JJA months) with similar anomaly structures, measured by the spatial anomaly

correlation coefficient (ACC). A set of dates with circulation analogues allows to calculate statistics conditionally to a given circulation [9,10,32,33], or to assess the role of dynamical changes in circulation-conditioned variables [11,12].

In order to estimate the contribution of dynamical changes to TXx and TXm trends (called hereafter the “dynamical TXx and TXm trends”), we replace each daily temperature field by those found for best analogue circulations in other dates of the time series. In the absence of long-term trends in circulation, this is equivalent to shuffling the temperature time series while keeping the dynamics, thereby creating a trend-free “analogue temperature time series”. In the presence of long-term circulation trends, the trend in the analogue temperature time series comes from the changes in circulations (e.g. an increase in circulations favorable to heat, or vice versa). Replacement by analogues should in principle remove thermodynamical effects from climate change. In order to ensure these were entirely removed, we further apply a correction by scaling all analogue temperatures to a reference year for global warming (2022) (see Methods). We verified that results were similar in both cases (not shown).

The dynamical TXm trend is found to exceed  $1^{\circ}\text{C}/\text{GWD}$  over Southwestern Europe (Fig 1b). The dynamical TXx trend (Fig 1d) reaches  $2^{\circ}\text{C}/\text{GWD}$  over Central France, and remains significant across Central Europe. Over Western Europe, the average TXm and TXx dynamical trends are respectively  $0.82^{\circ}\text{C}/\text{GWD}$  [ $0.33\text{-}1.32^{\circ}\text{C}/\text{GWD}$ ] and  $1.0^{\circ}\text{C}/\text{GWD}$  [ $0.39\text{-}1.64^{\circ}\text{C}/\text{GWD}$ ]. For E-OBS the dynamical trends are  $0.85^{\circ}\text{C}/\text{GWD}$  [ $0.34\text{-}1.37^{\circ}\text{C}/\text{GWD}$ ] and  $1.1^{\circ}\text{C}/\text{GWD}$  [ $0.44\text{-}1.69^{\circ}\text{C}/\text{GWD}$ ] for TXm and TXx respectively.

In order to verify our findings on extreme temperatures with another previously designed method, we also estimated the dynamical contributions to the trends using a second method, so-called “dynamical adjustment” [34] : The method uses a spatial circulation field (here: z500 for consistency with previous studies) as a proxy in order to estimate the contribution of circulation to temperature variability. Here, we use ridge regression, a linear regression technique that regularizes the coefficients of the high-dimensional circulation predictors [35], and we subsequently evaluate the dynamical contribution of z500 to the area-averaged Western Europe TXx trends (see method details in the Methods section). Results are consistent, with the analogue approach (Extended Data Figure 2), with however a weaker dynamical TXx trend of  $0.58^{\circ}\text{C}/\text{GWD}$  and a linear change of  $0.89^{\circ}\text{C}$  over 1950-2021.

Further, we investigate the specific streamfunction patterns associated with summer maximum extreme temperatures over central France [ $1.5\text{E};46.5\text{N}$ ] – i.e., in the region where the TXx dynamical trend is the largest (see Fig. 1). The highest TXx value at that location was reached on 29 June 2019 (an extreme temperature episode with  $40^{\circ}\text{C}$  largely exceeded in several places in Central France). We then select dates with ACC exceeding 0.5 with the streamfunction anomaly of 29/06/2019 (Fig. 2a). We find that about 15% of the summer days in total have an ACC larger than 0.5. For the sake of simplification, we will refer this class patterns as the “Southerly Flow” patterns (SF), since almost all of the patterns bear a positive west-east streamfunction gradient (eg. 99% of patterns when considering the gradient between  $15^{\circ}\text{W}$  and  $5^{\circ}\text{E}$  at  $50^{\circ}\text{N}$ ), inducing southerly flows over the Western margin of Europe. This pattern also

includes a strong anticyclonic component over Central Europe, which induces increased radiation and potential land-atmosphere feedbacks if persistent. As another example, the outstanding temperatures obtained in London on 19/07/2022 were also obtained with a similar circulation pattern (ACC=0.81 with 29/06/2019) (not shown).

To check how these days contribute to the dynamical trend, we recalculated the dynamical trend excluding the SF days: we removed SF days from the time series, calculated the analogue temperatures of remaining days, the resulting yearly TXx, and recalculated the dynamical trend. We also did the opposite operation by keeping only SF days in the time series. On average over Western Europe (Figure 2b), the dynamical TXx trend without SF patterns becomes insignificant over Western Europe ( $0.02^{\circ}\text{C}/\text{GWD}$  on average over Western Europe), while the SF-only TXx dynamical trend is high and significant ( $1.7^{\circ}\text{C}/\text{GWD}$ ). Note that along the analogue time series (in red in Fig. 2b), the contribution of SF flows to yearly TXx (red dots) become almost systematic in the latest part of the time series (typically since 2000). Dynamical TXx trends over Western Europe can therefore largely be explained by changes in the characteristics of SF patterns. First, their frequency has increased by 63% between 1950 and 2022, [+20%, +106%] (see Extended Data Figure 3). Second, the number of “events” (one event is defined here as a set of consecutive days) per year and their mean persistence have increased (see Extended Data Figure 3). The persistence of SF patterns has increased by about 45% along the period [+12%, +77%] as a function of GWD. Such changes all give more chance, within a season, to reach the high end of the conditional temperature distribution. Other characteristics may also have changed (eg. amplitude) but were not investigated here.

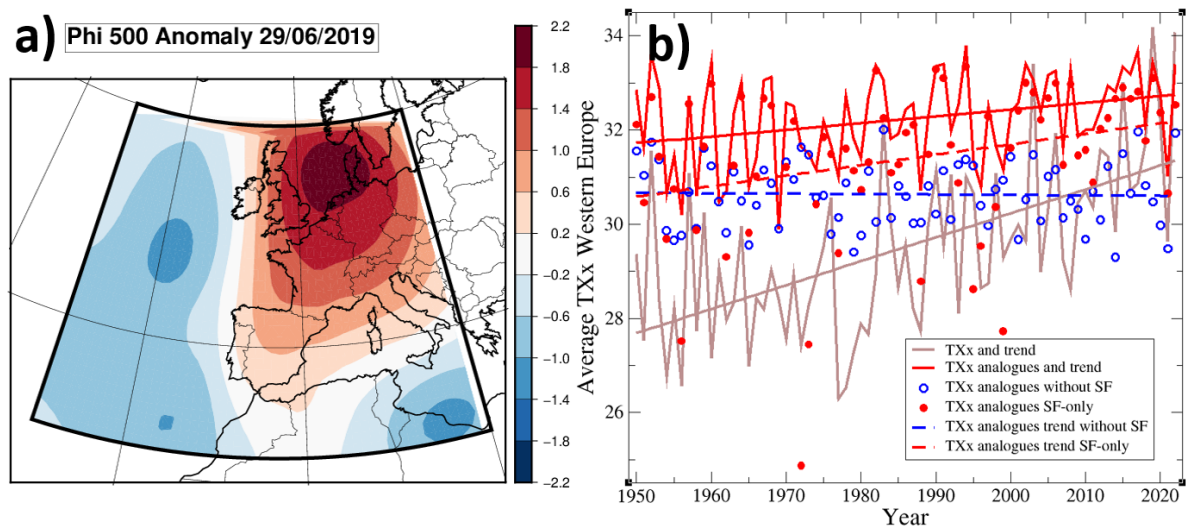


**Figure 2:** (left) Streamfunction anomaly of the 29/06/2019; (right) yearly time series of the Western Europe average of TXx (brown), the TXx of the analogue time series, averaged over Western Europe and the 3 best analogues (red curve) (see Methods), and the corresponding time series obtained by excluding (resp. including only) Southerly Flow (SF) pattern dates before calculating the analogue TXx values (blue circles, resp. red circles). The sets of dates (SF dates or non-SF dates) within a year over which the yearly maximum is sought are therefore complementary. In each case, analogues are calculated using the full set of patterns (i.e. for

non-SF dates, analogues may contain SF patterns). Linear trends for all series are also shown, with the same color as the series. The dashed red trend is that of the SF-only.

Note that SF is not the only flow pattern changing, and not all patterns associated with TXx days have an increasing frequency or persistence. For instance, the 23/07/2021 pattern, corresponding with summer TXx in central France for 2021, shows no particular evolution (Supp. Fig. 3). Our results are also consistent with the increase in occurrence and persistence of the specific class of double jet circulations explaining a large fraction of European heat extremes [3], and about half (i.e., much more than the mean probability, 15%) of double-jet days are found within the SF days. Vice versa we found that 15% of SF days are double jet days, which triples the probability of occurrence of double-jet days (5%).

The representation of summer TXx and TXm trends has then been analyzed for a large number of CMIP6 model simulations (273 simulations in total for 36 models) (see Methods section for data processing and Supplementary Information). Over Western Europe, almost all CMIP6 simulations fail to simulate the observed strong TXx trends, as seen in Figure 3b, plotting the percentage of simulations with larger trends than observed, for each grid point. These differences are less pronounced for seasonal mean summer temperatures (Fig. 3a) but the number of runs reaching the ERA5 trend remains small here too (10-20% in large parts of South-Western Europe). There are also other land areas outside Western Europe where the CMIP6 simulations are mostly above the observed warming trend (i.e. Sahara, Northern Scandinavia, Southern Balkans). This suggests that there is no general underestimation of extreme heat trends over all regions (or land regions), and that the Western Europe case is quite specific. However, understanding these regional discrepancies across the globe is beyond the scope of this article.

When averaging TXx trends over the Western Europe region above defined, only 4 of the 273 individual runs analyzed (one or two members of 3 models out of 36, ACCESS-ESM1, NorESM2-LM and KIOST-ESM) have a larger trend than the observations (see also Extended Data Figure 3). The strong TXx trends observed correspond to the ~98-99th percentile of the overall CMIP6 distribution and could, from a statistical standpoint, be interpreted as consistent with Western Europe witnessing a very unlikely phase of internal interdecadal variability. However, in the five large model ensembles that were at our disposal (eg. CanESM5, IPSL-CM6-LR, MIROC6, MPI-ESM1-2-LR, UK-ESM1-0-LL), only one (ACCESS-ESM1) has a few members that warm as rapidly as observed, but this ensemble strongly overestimate the mean summer trend (Figure 3c).

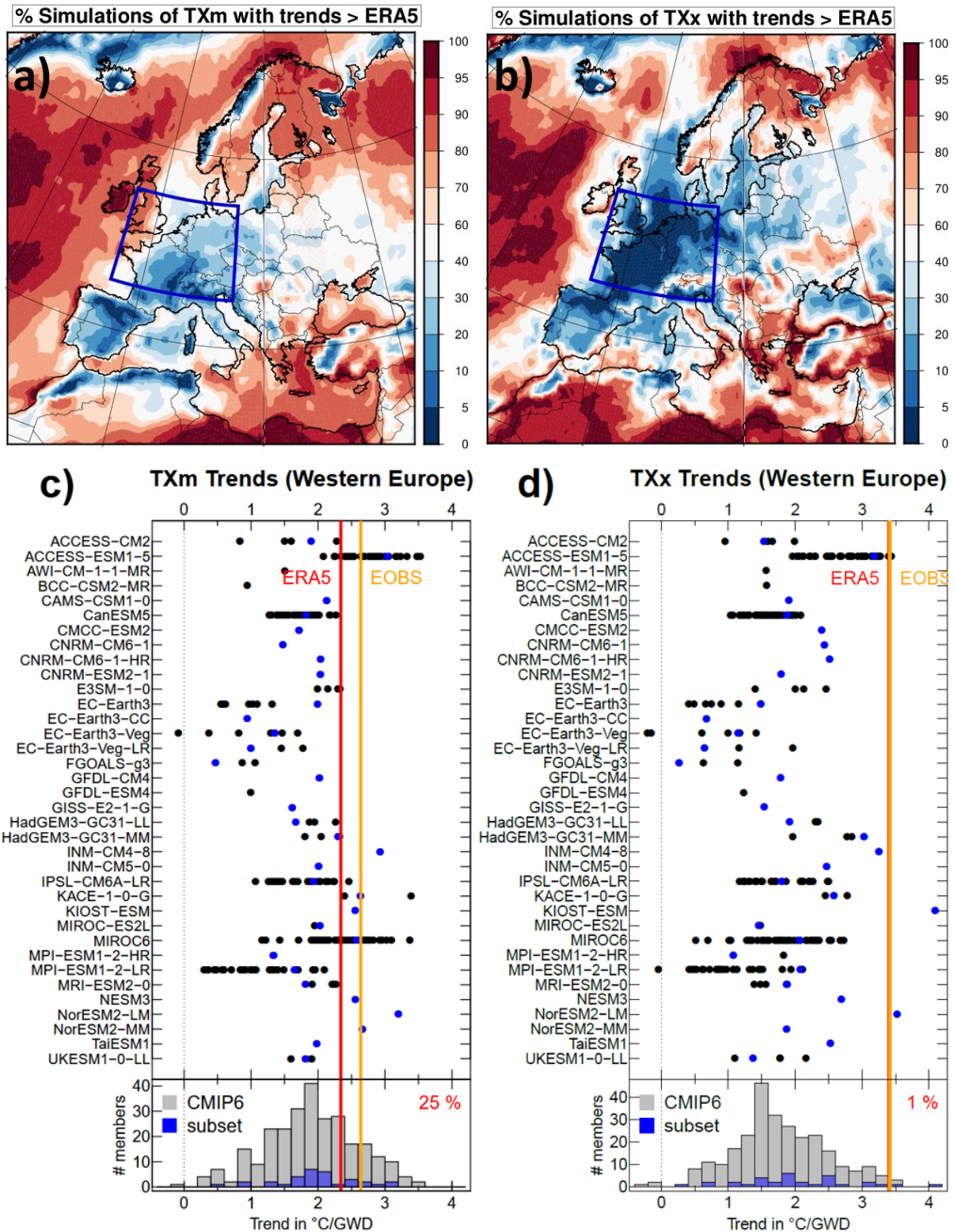


**Figure 3:** Comparison between ERA5 and 273 CMIP6 simulations of trends in Mean summer TX (TXm, left panels) and Maximum summer TX (TXx, right panels) in °C/GWD represented in different ways; top panels: percentage of simulations with a trend larger than ERA5 at each grid point; bottom panels: representation of trends for model ensembles (dots) and observations (red and orange lines) after averaging over Western Europe (5°W to 15°E ; 45°N-55°N); blue dots represent the simulations that were analyzed with the analogue approach. Histograms at the bottom of the figure summarize the overall distribution of the TXm (left) and TXx (right)



trends across the 273 simulations considered, together with the (blue) part analyzed with the analogue approach. Percentages of simulations with a trend larger than ERA5 are indicated in top right corners.

In addition, those climate simulations do not capture the dynamical changes underlying these temperature extreme changes. We applied the above analogue analysis to the first available realization for each model (to save computing and data handling and processing burden) for which 500 hPa wind fields were available (32 simulations in total). This set was found to be rather representative to the overall simulation distributions, see Figure 3c-d histograms) regarding temperature trends, with 2 models (KIOST-ESM and NorESM2-LM) exceeding trends similar to the observed ones for TXx, and 4-5 models with TXx trends only slightly below. None of these climate simulations reach the observed dynamical temperature trends with an amplitude as high as the observed one over western Europe (Figure 4a-b, top panels for the spatial distribution and Western Europe average for the bottom panels). On average over Western Europe, for summer mean (resp. maximum) trends, the highest amplitude of dynamical trends found in simulations reaches about  $0.18^{\circ}\text{C}/\text{GWD}$  (resp.  $0.45^{\circ}\text{C}/\text{GWD}$ ) (see Figure 4c and Extended Data Table 1) while observed values are typically about four times (resp. twice) higher. Among those simulations with relatively similar total TXx trends as ERA5, none exhibit a statistically significant dynamical trend. Thus, those simulations do capture the total trend observed but for the wrong reasons, i.e. they suffer from compensating biases between thermodynamical and dynamical processes.

We also calculated the thermodynamical trend obtained as a residual by subtracting the dynamical trend from the total trend. This shows that climate models exhibit thermodynamical contributions that are broadly consistent with ERA5, albeit with significant spread across models (Figs 4.c and 4.d, blue triangles). TXx thermodynamical trends can both be underestimated or overestimated across models, but there is a tendency for an overestimation of TXm thermodynamical trends, marked for models with rather correct total trend. This analysis clearly shows that dynamical changes are responsible for the systematic mismatch between modeled and observed temperature trends.

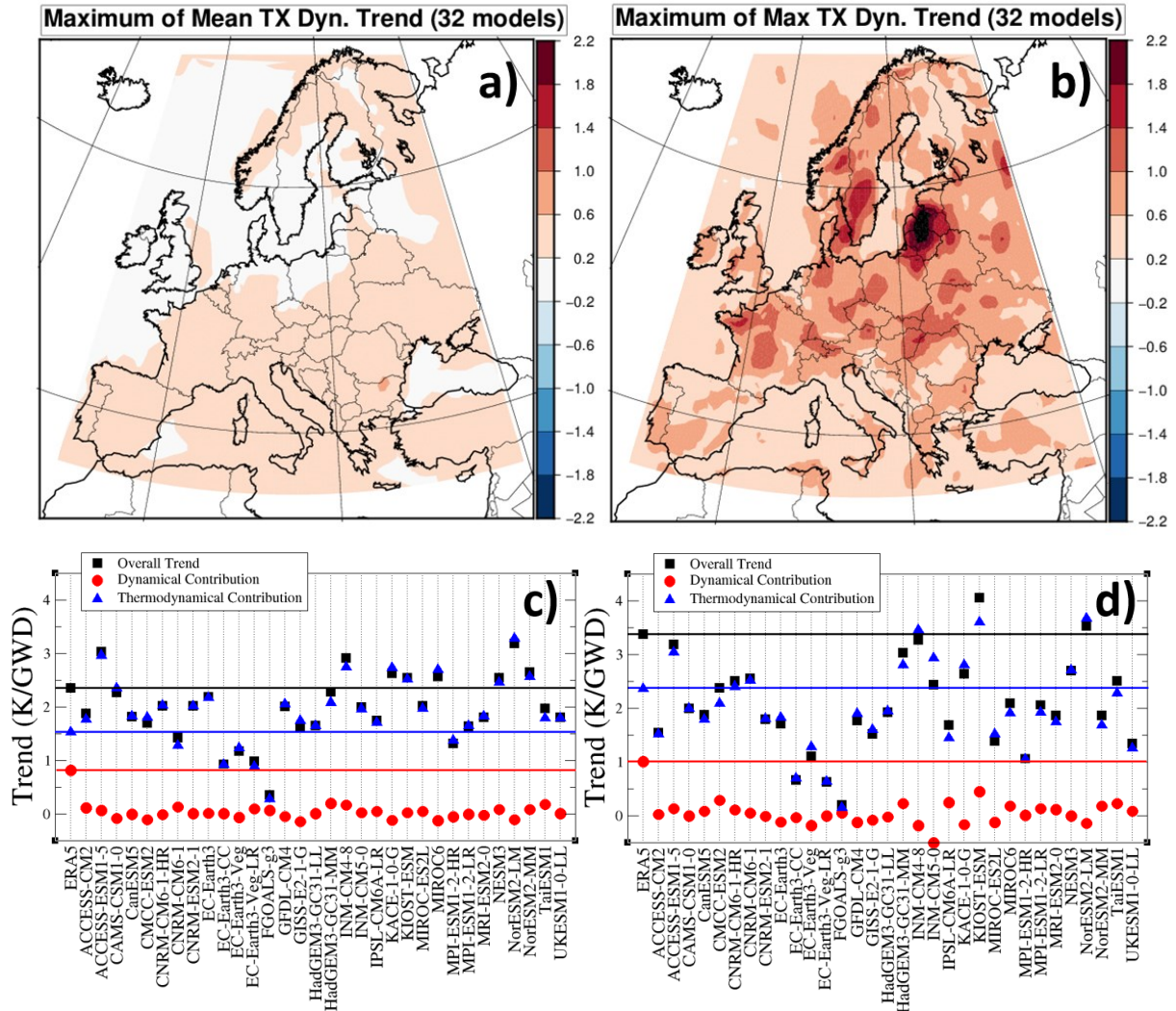


**Figure 4:** Upper panels: Maximum across 32 models of the dynamical contributions for trends (left: TXm; right: TXx); Lower panels: Total trend (black), dynamical contribution (red) and thermodynamical contribution from ERA5 (blue line), for the mean summer temperature (TXm, left panel) and yearly maximal temperature (TXx, right panel), averaged over Western Europe. The thermodynamical contributions are simply calculated as residual by subtracting the dynamical trend from the total trend. Confidence intervals are not shown here but can be found in Extended Data Table 1.

Climate simulations realistically simulate the climatological mean frequency of the SF patterns (range from 15% to 18%, see Supp. Table 1), with a slight overestimation compared to observations (14.6% for ERA5). However, the rapid observed increase in frequency of this flow field (+63% over 1950-2022 [20%-106%], or +57%/GWD [20%-93%]) is not simulated by any of the models. This is the prime reason why models fail to reproduce the over-proportioned trends in heat extremes. For most models there is even a decrease in the frequency of SF patterns, with sometimes large amplitudes (eg. a 20-30%/GWD decrease range for ACCESS-ESM1-5, CanESM5, MPI-ESM1-2-LR, NorESM2-MM; see Supp. Table 1). Event duration is also decreasing in most models.

Overall, our results show that CMIP6 models fail to reproduce the rapid observed warming of extreme heat over Western Europe. The analysis of atmospheric circulation changes shows that there is a large dynamical contribution to this observed trend, which is not reproduced by climate models, explaining a large part of the discrepancy in trend between models and observations. By contrast, models and observational trends are broadly consistent in terms of the thermodynamic contribution to the trend. We cannot rule out other sources of systematic uncertainties such as lack of homogeneity of reanalyses, in particular for circulation patterns, or inaccuracies in the aerosol and land use forcing changes that would translate in systematic model trend biases.

Determining the cause of the mismatch between models and observations is critical to assess whether the large observed warming trend is likely or unlikely to continue. If due to a wrong forced dynamical regional response – models underestimate the forced response to greenhouse gases – then this mismatch is expected to remain and even strengthen in the future, as global warming increases. If related to unforced internal variability [36,37] – internal variability simulated by models is too small – then the mismatch is expected to decrease in the future, but the term of this decrease is unknown and could be years or decades, leaving the fate of Western Europe heatwaves in large uncertainty.

Here we have shown that the observed extreme temperature trends for Western Europe are not captured by CMIP6 models, due to underestimated dynamical trends. Similar conclusions were found for wintertime weather over Europe [38]. Further research needs to determine the causes of the mismatch between simulated and observed temperature trends, whether this is due to uncaptured internal variability or missing (dynamical) forcing/processes. Either way, our results call for caution when using climate model projections for adaptation and resilience plans.

## Methods

**Calculation of dynamical contributions to mean and extreme summer temperature trends:** The method used to estimate dynamical contribution to the change in one variable follows the conceptual framework developed in Vautard et al. (2016), with a different implementation here. It is based on the estimation of the change in the variable solely due to the changes in regional upper-air circulations. For instance, even without extra heating from radiative and diabatic processes, an increase in the frequency of southerly flows in Western Europe would induce a mean regional warming. An increase in anticyclonic conditions would similarly lead to increased radiation and thus temperature. This can also lead to a cooling if increasingly frequent circulations are linked to cooler temperatures (eg. in Northerly winds). To estimate this dynamical effect of changing circulations on temperatures, we need to carefully remove any thermodynamical effect of climate change.

We assume that daily temperature  $T$  (which can be mean, minimum or maximum daily temperature, and in the current article will be maximum temperature) has a distribution at a given location or grid point which depends on the atmospheric circulation and on other processes, including global warming. We then assume a decomposition into:

$$(1) \quad T = \langle T|X \rangle_{GWD} + T' \quad ,$$

where  $X$  is the 500 hPa streamfunction anomaly, characterizing the atmospheric circulation (simultaneous to the temperature),  $GWD$  stands for the global warming degree,  $\langle T|X \rangle_{GWD}$  is the average daily maximum temperature conditioned to the circulation, assumed to be dependent on  $GWD$ , and  $T'$  is a fluctuation. This circulation-conditioned temperature includes not only advection effects (i.e. from cooler/warmer regions), but also all processes linked to the circulation (subsidence in anticyclone, increased radiation, surface-atmosphere feedbacks, ...), so the overall dynamical trend includes all underlying processes tied to the dynamical conditions. In order to remove thermodynamical effects due to climate change, we scale all temperatures to a reference warming level. For this, we assume that the circulation-conditioned mean temperature depends linearly on the global warming level, so the decomposition can be written:

$$(2) \quad T = \langle T|X \rangle_{ref} + b(X) \cdot (GWD - GWD_{ref}) + T' \quad ,$$

where  $ref$  refers to a reference global warming level, taken here as that of 2022, so all changes are expressed relative to 2022. The coefficient  $b(X)$  represents the mean warming rate conditioned to the circulation  $X$ , which includes thermodynamical effects of the climate change response – it is therefore assumed that the amount of warming depends on the circulation type. Assuming one can calculate  $b(X)$  and  $GWD$ , all daily temperatures are then scaled to the reference level with the following thermodynamical correction:

$$T_s = T - b(X) \cdot (GWD - GWD_{ref}) \quad (3)$$

The dynamical contribution to any temperature trend constructed from daily temperatures (eg. here TXm, TXx) can then be calculated from the  $T_s$  time series, because changes with *GWD* are only through the changes in the frequency of occurrences of  $X$  for given *GWD*s. Trends should also not depend on the particular time  $T_s$  values are drawn as long as they occur simultaneously to a streamfunction anomaly which is similar to that encountered in the same sequence order as that of the series. Hence to increase statistical robustness and remove any residual link to the specific order of temperatures, we replace  $T_s$  temperatures by those occurring in circulations  $X$  along the time series. This has the advantage of “randomizing” the timing of analogues and providing multiple realizations to calculate dynamical trends. A new temperature analogue series is created by replacing each daily with that of the best circulation analogue, then another new series is made with the second best analogue, etc... (see below for practical analogue calculation). From each of these analogue time series, TXm and TXx are recalculated for each year, then averaged across analogues, and a regression with *GWD* is calculated at each grid point, together with its confidence interval, (plus or minus twice the standard error of the regression coefficient). To keep analogue quality high, we limit the number of time series to 3. To calculate time series of averages over Western Europe land, we apply the  $0.5^\circ \times 0.5^\circ$  land mask of E-OBS and average over the grid points included in  $[-5W - 15E ; 45N - 55N]$

**Estimation of yearly *GWD*** : In practice, *GWD* is calculated as a moving centered 5-year average of the global temperature with available data, for reanalyses and models, accounting for series ends in ERA5 (i.e. for 1950, taking into account an average only over 1950 to 1952, and for 2022 an average over 2020 and 2021). The 2022 value is then subtracted to all values, so *GWD* is 0 in 2022, and generally negative before.

**Selection of circulation analogues** : In practice, circulations are characterized by the 500 hPa streamfunction over the  $[-30 +20^\circ E ; 30 60^\circ N]$  domain. Analogs of a given circulation are characterized by anomaly correlation coefficient (ACC) between streamfunction fields. For each summer day, we collect the best analogues (highest ACCs), and impose that they remain spaced by 6 days or more within a season, and self-analogues are not considered. This is done by successively testing fields in descending order of the ACC, and skipping days not respecting the separation with previously selected fields.

**Calculation of the circulation-conditioned thermodynamical trend  $b(X)$**  : To calculate  $b(X)$ , we also use analogue circulations, in a different way than above: For each summer day  $d$  of the 1950-2022 period, we estimate  $b(X(d))$  using a regression of each raw temperature  $T(d)$  (before thermodynamical correction) associated with a large set of best analogue circulations of  $X(d)$  found between 1950 and 2022 with the *GWD* values of their respective year. We use the best 1% summer analogues (67 days) with the same spacing of at least 6 days. 99% of the worst of these 67 analogues across all summer days have  $ACC > 0.5$ , 65% have  $ACC > 0.7$ . Imposing a quality criterion on analogues such as  $ACC > 0.7$  or more would leave days with an insufficient number of analogues for regression.

**Dynamical adjustment:** Dynamical adjustment is used as a second, alternative technique to estimate the influence of circulation-induced temperature trends. The method relies on the idea that temperature variability can be decomposed into a component that is driven by circulation-induced variability, and a residual, thermodynamical component. The latter “thermodynamical” component is expected to contain a forced signal as well as any other unexplained variability or feedbacks [39]. Most applications of the technique characterize circulation-induced temperature variability using a proxy variable [34,35,40,41]. Dynamical adjustment techniques typically rely on linear methods such as variants of linear regression or circulation analogue techniques.

Here, we use the spatial pattern of z500 in a relatively large circulation domain over Europe and the North Atlantic (-30 to 20°E, 30 to 60°N, similar to Fig. 1). We broadly follow the method outlined in [42], but add some details and small modifications here: We use a regularized regression technique, called “ridge regression”, which is well-suited to deal with the large number of circulation predictor grid cells ( $p = X$ ) and a relatively short observed record. For TX<sub>x</sub>, we train our method on the 15 warmest days in each summer during 1950-2021 in the ERA5 reanalysis (thus the training sample consists in a total of 72 summers and 15 days per summer). Because the z500 field contains information about the lower troposphere, and is affected by temperature change via thermal expansion, we detrend the spatial z500 field by subtracting the global average z500 at each time step and over each grid cell in the circulation domain. Hence, the analysis is based only on relative changes within the z500 field.

## **Acknowledgements**

This study was partly supported by the European Union's Horizon 2020 research and innovation programme under grant agreement No 101003469 (XAIDA project). PY was also supported by the grant ANR-20-CE01-0008-01 (SAMPRACE). The authors thank Dr. Efi Rousi for providing the sequences of dates of double-jet days. The authors also thank Atef Ben Nasser and the ESPRI IPSL data and computing service for their support in handling the large ensemble of climate simulations.

## **Authors contributions**

R.V., J.C. and J. S. carried out the statistical analysis. T. H. provided the streamfunction fields for ERA5 and the calculation method. All other authors contributed to the design of the study and the interpretation of results. All authors contributed to the writing of the article.

## References

- [1] Seneviratne, S.I., et al. [Masson-Delmotte, et al. (eds.)]. Cambridge University Press, Cambridge, United Kingdom and New York, NY, USA, pp. 1513–1766 (2021).
- [2] Robinson, A. et al. Increasing heat and rainfall extremes now far outside the historical climate. *npj Clim Atmos Sci* 4, 45 (2021).
- [3] Rousi, E., Kornhuber, K., Beobide-Arsuaga, G., Luo, F., & Coumou, D. Accelerated western European heatwave trends linked to more-persistent double jets over Eurasia. *Nature communications*, 13(1), 1-11 (2022).
- [4] van Oldenborgh, et al. Western Europe is warming much faster than expected, *Clim. Past*, 5, 1–12, <https://doi.org/10.5194/cp-5-1-2009> (2009).
- [5] van Oldenborgh, et al. Attributing and projecting heatwaves is hard: we can do better. *Earth's Future*, 10(6), e2021EF002271 (2022).
- [6] Vautard, R., et al. Human contribution to the record-breaking June and July 2019 heatwaves in Western Europe. *Environmental Research Letters*, 15(9), 094077 (2020).
- [7] Bo e, J., et al. Past long-term summer warming over western Europe in new generation climate models: role of large-scale atmospheric circulation. *Environmental Research Letters*, 15(8), 084038 (2020).
- [8] Ribes, A., et al. An updated assessment of past and future warming over France based on a regional observational constraint. *Earth System Dynamics Discussions*, 1-29 (2022).
- [9] Yiou, P., Vautard, R., Naveau, P., & Cassou, C. Inconsistency between atmospheric dynamics and temperatures during the exceptional 2006/2007 fall/winter and recent warming in Europe. *Geophysical Research Letters*, 34(21) (2007).
- [10] Cattiaux, J., et al. Winter 2010 in Europe: A cold extreme in a warming climate. *Geophysical Research Letters*, 37(20) (2010).
- [11] Vautard, R., & Yiou, P. Control of recent European surface climate change by atmospheric flow. *Geophysical Research Letters*, 36(22) (2009).
- [12] Vautard, R., et al. Attribution of human-induced dynamical and thermodynamical contributions in extreme weather events. *Environmental Research Letters*, 11(11), 114009 (2016).



- [13] García-Herrera, R., Díaz, J., Trigo, R. M., Luterbacher, J., & Fischer, E. M. A review of the European summer heat wave of 2003. *Critical Reviews in Environmental Science and Technology*, 40(4), 267-306 (2010).
- [14] Yiou, P., et al. Analyses of the Northern European summer heatwave of 2018. *Bulletin of the American Meteorological Society*, 101(1), S35-S40 (2020).
- [15] McCarthy, M., Christidis, N., Dunstone, N., Fereday, D., Kay, G., Klein-Tank, A., ... & Stott, P. Drivers of the UK summer heatwave of 2018. *Weather*, 74(11), 390-396 (2019).
- [16] <https://www.worldweatherattribution.org/without-human-caused-climate-change-temperatures-of-40c-in-the-uk-would-have-been-extremely-unlikely/>
- [17] Fischer, E.M., Sippel, S. & Knutti, R. Increasing probability of record-shattering climate extremes. *Nat. Clim. Chang.* 11, 689–695 (2021).
- [18] Lorenz, R., Stalhandske, Z., & Fischer, E. M. Detection of a climate change signal in extreme heat, heat stress, and cold in Europe from observations. *Geophysical Research Letters*, 46(14), 8363-8374 (2019).
- [19] Hersbach, H., et al. The ERA5 global reanalysis. *Quarterly Journal of the Royal Meteorological Society*, 146(730), 1999-2049 (2020).
- [20] Cornes, R. C., van der Schrier, G., van den Besselaar, E. J., & Jones, P. D. An ensemble version of the E-OBS temperature and precipitation data sets. *Journal of Geophysical Research: Atmospheres*, 123(17), 9391-9409 (2018).
- [21] Hoogeveen, J., & Hoogeveen, H. Winds are changing: An explanation for the warming of the Netherlands. *International Journal of Climatology* (2022).
- [22] Nabat, P., Somot, S., Mallet, M., Sanchez-Lorenzo, A., & Wild, M. Contribution of anthropogenic sulfate aerosols to the changing Euro-Mediterranean climate since 1980. *Geophysical Research Letters*, 41(15), 5605-5611 (2014).
- [23] Stegehuis, A. I., et al. Early summer soil moisture contribution to Western European summer warming. *Journal of Geophysical Research: Atmospheres*, 126(17), e2021JD034646 (2021).
- [24] Coumou, D., Lehmann, J., & Beckmann, J. The weakening summer circulation in the Northern Hemisphere mid-latitudes. *Science*, 348(6232), 324-327 (2015).
- [25] Terray, L. A dynamical adjustment perspective on extreme event attribution. *Weather and Climate Dynamics*, 2(4), 971-989 (2021).

- [26] Horton, D. E., et al. Contribution of changes in atmospheric circulation patterns to extreme temperature trends. *Nature*, 522(7557), 465-469 (2015).
- [27] Faranda, D., Messori, G., Jézéquel, A., Vrac, M., Yiou, P.. Atmospheric circulation compounds anthropogenic warming and extreme climate impacts in Europe. Under Review, 2022. (hal-03456537v2)
- [28] Fery, L., Dubrulle, B., Podvin, B., Pons, F., & Faranda, D. Learning a weather dictionary of atmospheric patterns using Latent Dirichlet Allocation. *Geophysical Research Letters*, 49(9), e2021GL096184 (2022).
- [29] Davini, P., & d'Andrea, F. From CMIP3 to CMIP6: Northern Hemisphere atmospheric blocking simulation in present and future climate. *Journal of Climate*, 33(23), 10021-10038 (2020).
- [30] Kornhuber, K., et al. Extreme weather events in early summer 2018 connected by a recurrent hemispheric wave-7 pattern. *Environmental Research Letters*, 14(5), 054002 (2019).
- [31] Suarez-Gutierrez, L., Li, C., Müller, W. A., & Marotzke, J. Internal variability in European summer temperatures at 1.5 C and 2 C of global warming. *Environmental Research Letters*, 13(6), 064026 (2018).
- [32] Jézéquel, A., Yiou, P., & Radanovics, S. Role of circulation in European heatwaves using flow analogues. *Climate dynamics*, 50(3), 1145-1159 (2018).
- [33] Faranda, et al. A climate-change attribution retrospective of some impactful weather extremes of 2021, *Weather Clim. Dyn.*, 3, 1311–1340, <https://doi.org/10.5194/wcd-3-1311-2022> (2022).
- [34] Deser, C., A. Phillips, M. A. Alexander, and B. V. Smoliak. Projecting North American climate over the next 50 years: Uncertainty due to internal variability. *J. Climate*, 27, 2271–2296 (2014).
- [35] Sippel, S., et al. Uncovering the forced climate response from a single ensemble member using statistical learning. *Journal of Climate*, 32(17), 5677-5699 (2019).
- [36] Qasmi, S., Cassou, C., & Boé, J. Teleconnection between Atlantic multidecadal variability and European temperature: Diversity and evaluation of the Coupled Model Intercomparison Project phase 5 models. *Geophysical Research Letters*, 44(21), 11-140 (2017).
- [37] McKinnon, K. A., & Deser, C. Internal variability and regional climate trends in an observational large ensemble. *Journal of Climate*, 31(17), 6783-6802 (2018).

- [38] Blackport, R., & Fyfe, J. C. Climate models fail to capture strengthening wintertime North Atlantic jet and impacts on Europe. *Science Advances*, 8(45), eabn3112 (2022).
- [39] Merrifield, A., F. Lehner, S.-P. Xie, and Deser, C. Removing circulation effects to assess central US land–atmosphere interactions in the CESM large ensemble. *Geophys. Res. Lett.*, 44, 9938–9946 (2017).
- [40] Smoliak, B. V., J. M. Wallace, P. Lin, and Fu, Q. Dynamical adjustment of the Northern Hemisphere surface air temperature field: Methodology and application to observations. *J. Climate*, 28, 1613–1629 (2015).
- [41] Saffioti, C., E. M. Fischer, and Knutti, R. Improved consistency of climate projections over Europe after accounting for atmospheric circulation variability. *J. Climate*, 30, 7271–7291 (2017).
- [42] Sippel, S., Meinshausen, N., Fischer, E. M., Székely, E., & Knutti, R. Climate change now detectable from any single day of weather at global scale. *Nature climate change*, 10(1), 35-41 (2020).

# Supplementary Information

## Observation and model data

We used ERA5 reanalysis of daily maximum temperatures and streamfunction fields. Streamfunction is calculated from  $u$ - and  $v$ - wind fields at 500 hPa on a T127 Gaussian grid, and then interpolated on a 1x1 regular grid, following:

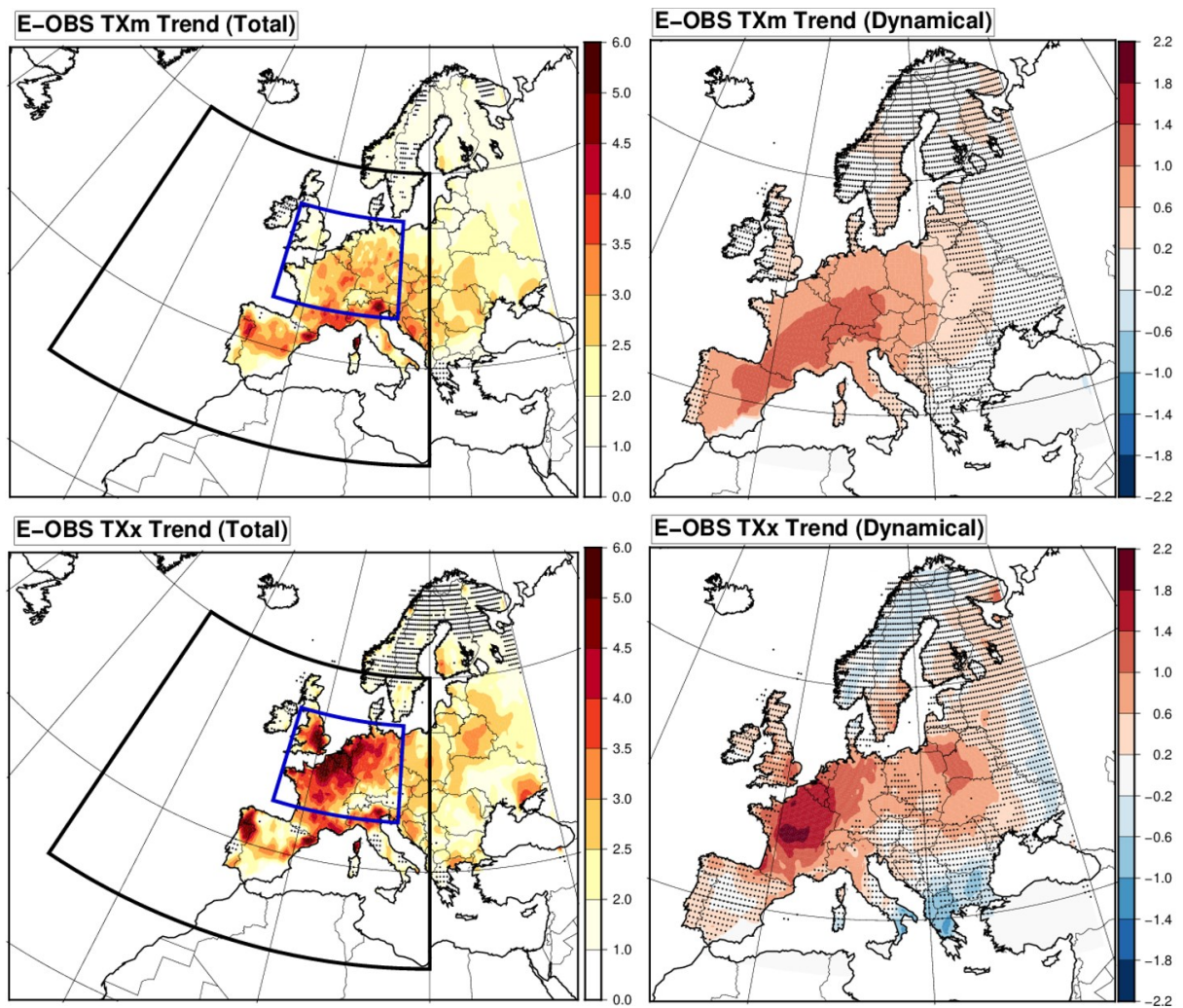
$u = -\frac{\partial\psi}{\partial y}$ , and  $v = \frac{\partial\psi}{\partial x}$ , where  $\psi$  is the streamfunction,  $u$  is the zonal- and  $v$  the meridional component of the wind fields.

Surface daily maximum temperatures from ERA5 are interpolated to a 0.5x0.5 grid. We also used observations from the E-OBS dataset v24e [20] for daily maximum temperature (TX). E-OBS was initially taken from a 0.25 x 0.25 grid and projected onto the 0.5x0.5 grid. When considering averages over the selected Western Europe area [5W-15E;45N-60N], data are masked using the E-OBS land/sea mask (see below).

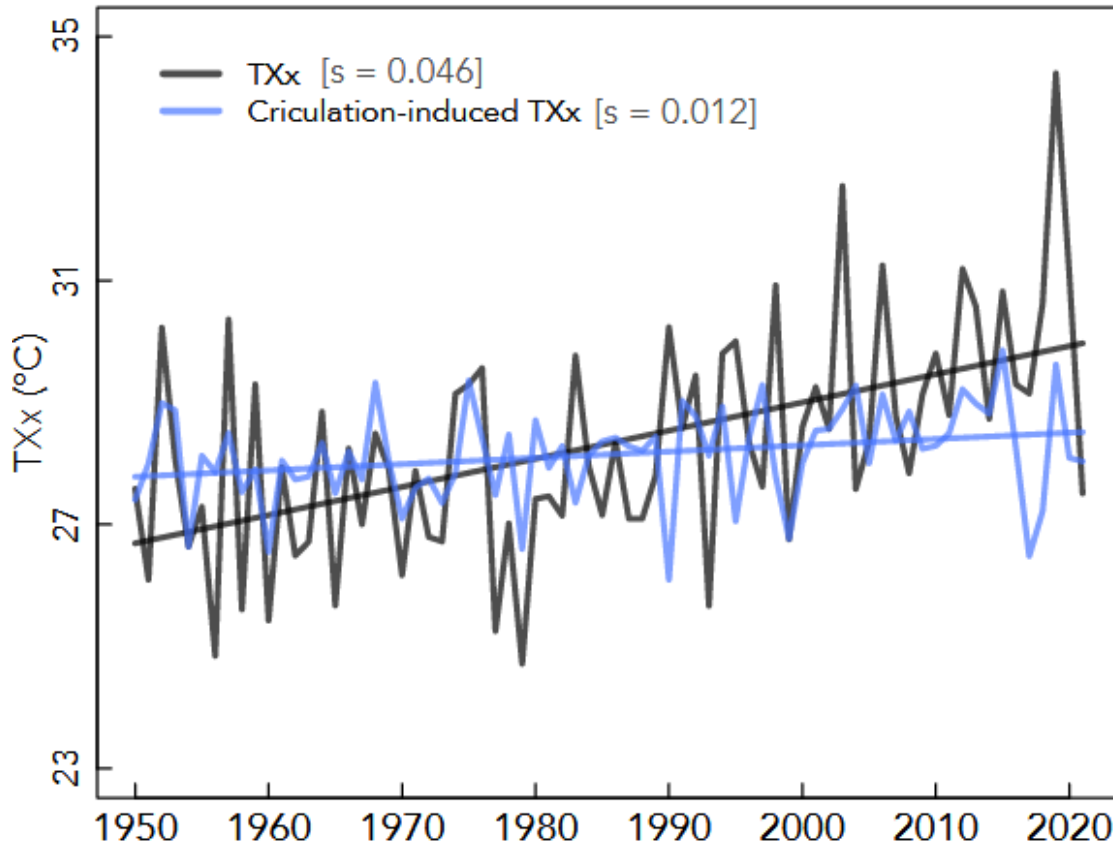
Daily maximum temperatures and streamfunction are also calculated from model simulations including all first members of each CMIP6 model ensemble. In order to increase as much as possible the estimation of capacity of models to simulate TXx and TXm trends, we used all possible CMIP6 simulations made available through the ESGF infrastructure. When considering only TXx and TXm calculations for Figure 3, we used 273 simulations made with 36 different models (see Figure 3). For Figure 4 and the analogue analysis for models, we keep only 32 models and 1 realization for which we have simultaneous 500 hPa wind fields and daily maximum temperatures.

To have an historical time series to be compared with reanalysis or observations, we concatenate historical and SSP5-8.5 scenarios available (from 2015 to 2022). Initial tests made with SSP2-4.5 showed that results presented here are insensitive to this choice.

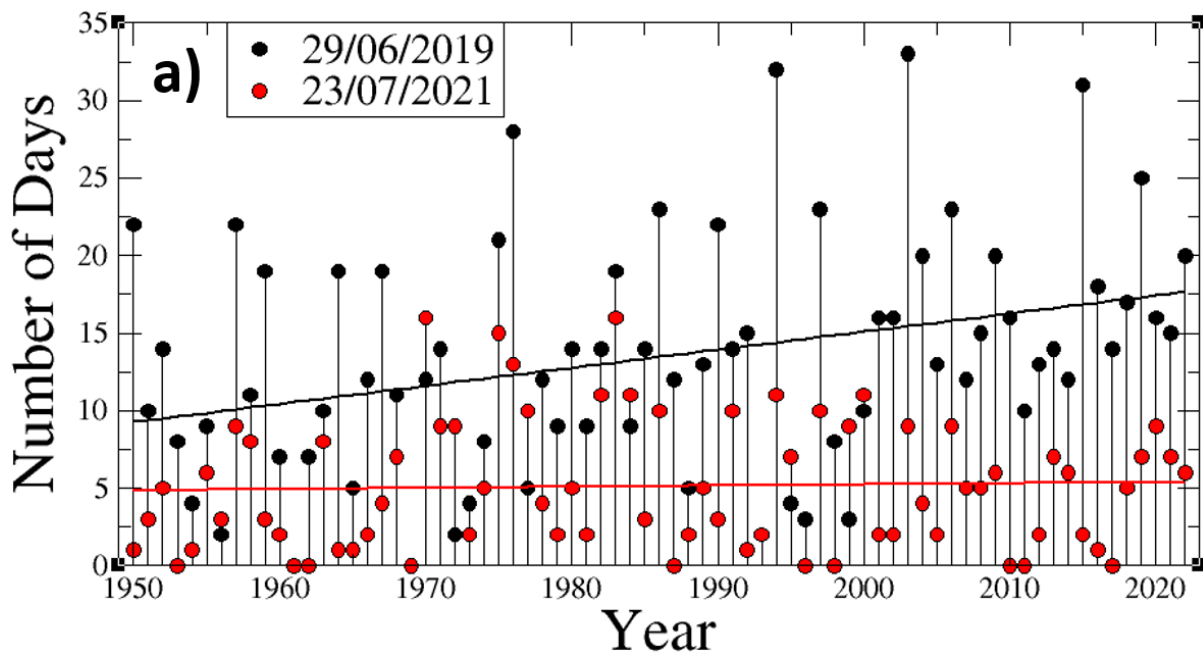
## Extended Data Figures

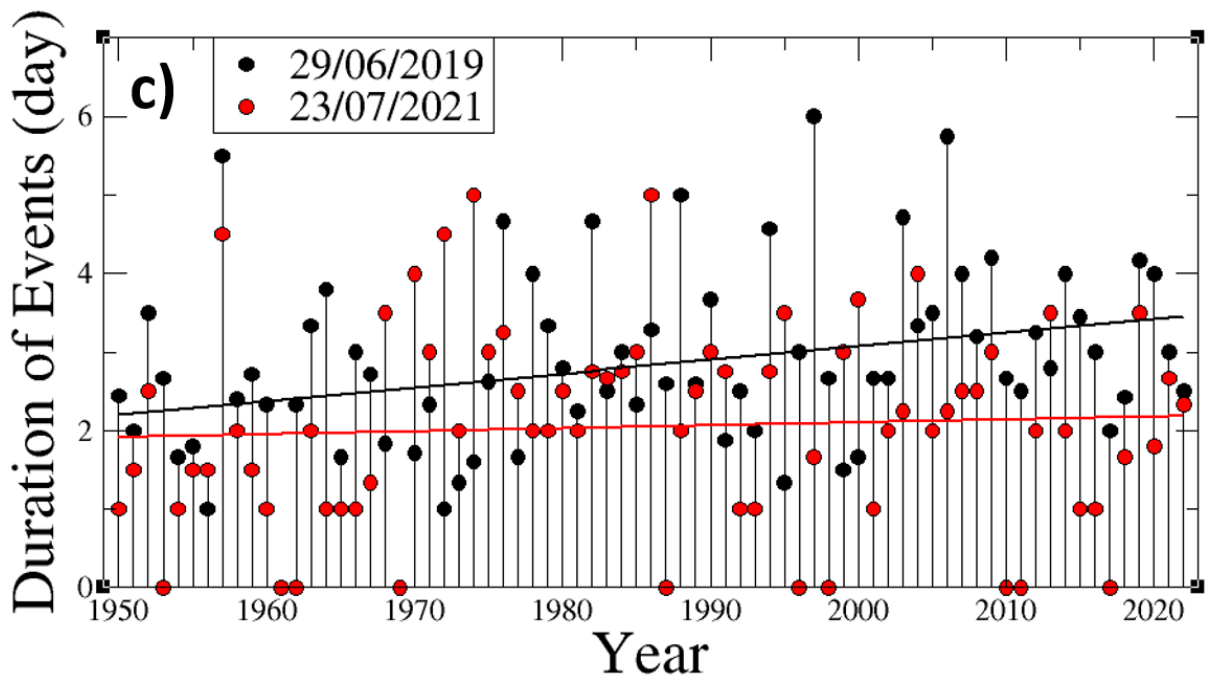
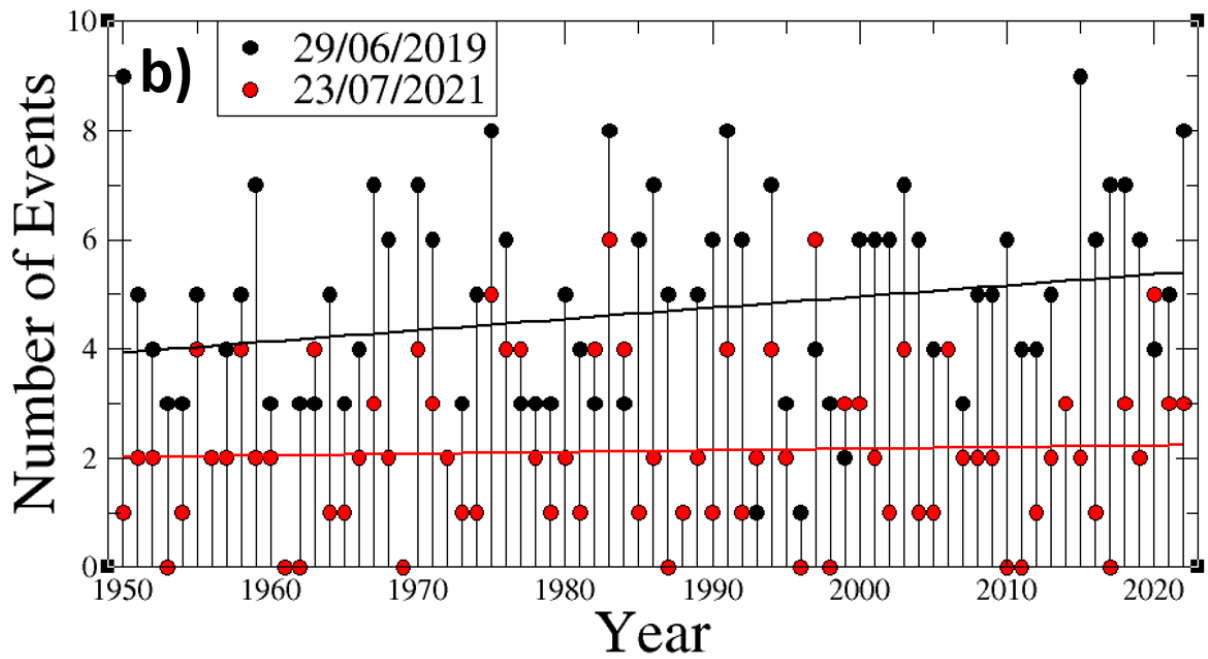


**Extended Data Figure 1:** Same as Figure 1 but for E-OBS maximum daily temperatures



**Extended Data Figure 2:** Dynamical contribution to forced trend during 1950–2021 in ERA5 reanalysis. Black and blue lines present the area-averaged TXx and circulation-induced TXx over western Europe (5–15E, 45–55N), respectively. The numbers in the square bracket show the trend ( $^{\circ}\text{C}/\text{season}$ ) in the corresponding TXx time series. The trends are estimated based on Sen’s slope estimator.





**Extended Data Figure 3:** Evolution of the yearly number of days (a), number of events (b) and mean duration of events (c) (0 when no event found) for Southerly Flow patterns (black) (streamfunction anomalies with an ACC with the 29/06/2019 anomaly greater than 0.5). For comparison, the figure also shows (in red) the same statistics but for another pattern (not shown), that of the anomaly of the 23/07/2021, which corresponds to the date of TXx for 2021 in central France.

Model_realization	Dynamical trend TXm (°C/GWD)	Dynamical trend TXx (°C/GWD)	Frequency SF %	Frequency SF change in %/GWD	Duration SA change in %/GWD
<b>ERA5</b>	<b>0.82 [ 0.33 1.32]</b>	<b>1.01 [ 0.39 1.64]</b>	<b>14.6</b>	<b>57 [20 93]</b>	<b>39 [11 67]</b>
ACCESS-CM2_r1i1p1f1	0.12 [-0.05 0.29]	0.03 [-0.30 0.35]	17.4	-13 [-34 8]	-14 [-29 1]
ACCESS-ESM1-5_r2i1p1f1	0.08 [-0.08 0.23]	0.14 [-0.18 0.46]	17.1	-30 [-54 -6]	-8 [-24 8]
CAMS-CSM1-0_r2i1p1f1	-0.08 [-0.50 0.34]	0.00 [-0.73 0.73]	16.6	-27 [-69 14]	-8 [-41 25]
CanESM5_r1i1p1f1	0.00 [-0.12 0.12]	0.09 [-0.08 0.25]	17.3	-21 [-38 -5]	-2 [-12 9]
CMCC-ESM2_r1i1p1f1	-0.10 [-0.26 0.06]	0.29 [-0.19 0.78]	17.9	8 [-15 30]	11 [-4 25]
CNRM-CM6-1-HR_r1i1p1f2	-0.01 [-0.24 0.22]	0.11 [-0.24 0.46]	15.8	7 [-20 34]	5 [-18 29]
CNRM-CM6-1_r1i1p1f2	0.14 [-0.06 0.34]	0.05 [-0.28 0.38]	17.1	0 [-28 28]	9 [-12 30]
CNRM-ESM2-1_r1i1p1f2	0.01 [-0.18 0.20]	-0.01 [-0.25 0.22]	16.7	-1 [-20 18]	1 [-16 18]
EC-Earth3_r1i1p1f1	0.02 [-0.10 0.14]	-0.11 [-0.44 0.23]	16.8	-10 [-29 9]	-1 [-14 12]
EC-Earth3-CC_r1i1p1f1	0.01 [-0.11 0.13]	-0.03 [-0.30 0.24]	17.1	-6 [-26 14]	-5 [-24 14]
EC-Earth3-Veg_r1i1p1f1	-0.06 [-0.24 0.11]	-0.18 [-0.54 0.19]	17.4	-5 [-27 17]	-11 [-26 5]
EC-Earth3-Veg-LR_r1i1p1f1	0.10 [-0.09 0.28]	0.00 [-0.41 0.42]	17.3	-10 [-40 19]	-12 [-31 8]
FGOALS-g3_r1i1p1f1	0.07 [-0.08 0.23]	0.05 [-0.21 0.30]	17.9	-19 [-41 3]	-13 [-29 4]
GFDL-CM4_r1i1p1f1	-0.04 [-0.17 0.09]	-0.12 [-0.37 0.13]	17.3	-3 [-22 16]	2 [-14 17]
GISS-E2-1-G_r1i1p1f2	-0.14 [-0.32 0.05]	-0.08 [-0.43 0.26]	15.8	-1 [-38 25]	-10 [-26 7]
HadGEM3-GC31-LL_r1i1p1f3	0.01 [-0.11 0.14]	-0.02 [-0.29 0.24]	17.3	-19 [-36 -2]	-14 [-26 -2]
HadGEM3-GC31-MM_r1i1p1f3	0.20 [0.04 0.36]	0.23 [-0.21 0.66]	16.0	-15 [-40 10]	-14 [-30 2]
INM-CM4-8_r1i1p1f1	0.17 [-0.14 0.48]	-0.18 [-0.71 0.35]	15.2	-19 [-47 10]	-9 [-27 9]
INM-CM5-0_r1i1p1f1	0.03 [-0.36 0.42]	-0.50 [-0.97 -0.02]	16.3	-14 [-43 14]	3 [-19 25]
IPSL-CM6A-LR_r1i1p1f1	0.05 [-0.10 0.20]	0.25 [0.02 0.49]	16.0	-5 [-25 16]	-17 [-36 1]
KACE-1-0-G_r1i1p1f1	-0.11 [-0.30 0.08]	-0.16 [-0.52 0.21]	16.9	-20 [-38 -1]	-15 [-28 -2]
KIOST-ESM_r1i1p1f1	0.03 [-0.13 0.18]	0.45 [-0.01 0.90]	18.1	-2 [-23 19]	3 [-11 16]
MIROC-ES2L_r1i1p1f2	0.05 [-0.17 0.26]	-0.12 [-0.54 0.30]	17.3	6 [-26 37]	-2 [-25 20]
MIROC6_r1i1p1f1	-0.12 [-0.43 0.19]	0.18 [-0.30 0.67]	17.3	-19 [-57 18]	12 [-15 39]
MPI-ESM1-2-HR_r1i1p1f1	-0.05 [-0.22 0.11]	0.01 [-0.37 0.39]	16.9	-9 [-35 16]	-9 [-29 10]
MPI-ESM1-2-LR_r1i1p1f1	0.00 [-0.11 0.12]	0.14 [-0.18 0.47]	16.3	-27 [-53 -1]	-23 [-51 5]
MRI-ESM2-0_r1i1p1f1	-0.02 [-0.18 0.14]	0.12 [-0.18 0.41]	17.9	3 [-18 24]	12 [-7 31]
NESM3_r1i1p1f1	0.09 [-0.08 0.27]	-0.00 [-0.20 0.20]	16.8	-7 [-27 13]	-1 [-17 15]
NorESM2-LM_r1i1p1f1	-0.10 [-0.28 0.08]	-0.14 [-0.66 0.38]	17.5	-13 [-35 10]	-19 [-38 -0]
NorESM2-MM_r1i1p1f1	0.09 [-0.12 0.30]	0.18 [-0.16 0.52]	17.0	-28 [-52 -4]	0 [-21 21]
TaiESM1_r1i1p1f1	0.18 [0.01 0.36]	0.23 [-0.16 0.62]	17.9	-8 [-31 14]	-2 [-19 14]
UKESM1-0-LL_r1i1p1f2	0.01 [-0.12 0.13]	0.09 [-0.15 0.33]	16.8	-23 [-40 -7]	-9 [-22 4]

**Extended Data Table 1:** Models used for the dynamical temperature trend analysis (and reanalysis, first line); the name indicates the model and the realization, with ssp585 concatenated after 2014 to historical simulation in order to have a continuous time series from 1950 to 2022; Second column: summer TXm trend averaged over the land Western Europe area [5W;15E;45N;55N], and its confidence interval (calculated as +/-2 S.E. of the regression coefficient of the spatial average vs. the GWD of each simulation); Third column: same as the second for summer TXx; Fourth column: frequency of Southerly Flow patterns (SF) defined as the class of patterns with streamfunction anomaly correlation larger than 0.5 with that of 29/06/2019 (Figure 3a); Fifth column: frequency change over 1950-2022 as a function of the GWD, together with the confidence interval, calculated as a regression of the mean yearly frequency with GWD; Sixth column, same as Fifth column for persistence change, calculated from mean yearly duration of event regressed with the GWD, and the confidence interval calculated as above.